



# Zirconia-Based Nanomaterials for Alternative Energy Application: Concept of Research in Smart Laboratory

Anton Gorban<sup>1</sup> · Artem Shylo<sup>2</sup> · Viktoriia Dmitrenko<sup>2</sup> · Sergii Tsololo<sup>1</sup> · Leonid Akhkozov<sup>2</sup> · Valery Burkhovetsky<sup>2</sup> · Olesya Shapovalova<sup>3</sup> · Oksana Gorban<sup>2</sup> · Igor Danilenko<sup>2</sup>

Received: 14 December 2021 / Accepted: 15 May 2022 / Published online: 20 June 2022  
© King Fahd University of Petroleum & Minerals 2022

## Abstract

The engineering of doped zirconia nanoparticles (NPs) for energy application is realized in concept Research Smart Laboratory. To improve nanomaterials' engineering, correlations of “salt concentration—powder dispersity” and “calcined temperature—particle's sizes” were built. The correlation of “materials structure—materials functionality” is made. The technology forming ceramics with varying grain sizes and densities under the same thermodynamic conditions (1350 °C) from NPs with different sizes is developed. The impedance spectroscopy with the distribution of relaxation time analysis is used for ionic conductivity ceramic investigation in range 240–900 °C. The activation energies of the grain and grain boundary oxygen diffusion are calculated. It was shown that the energy activation of bulk oxygen diffusion does not depend on ceramic grain size ( $E_a = 0.9$  eV). The energies activation of grain boundary oxygen diffusion estimated in the framework of the bricklayer model show a weak growth with the rising of ceramic grains sizes. The values of the volume activation energy are close to the grain-boundary activation energy for ceramics obtained from nanoparticles smaller than 18 nm. It was found that the grain boundary space contains two types of elements with different geometries. The size of NPs used for ceramic determines the size of grain boundaries elements. It was shown that the density of sintered ceramic has a more substantial effect on its electrophysical properties than grain size. The NPs sizes of 18–24 nm are optimal for forming pressed powder compacts and sintered ceramics with high density.

**Keywords** SmartLab concept · Zirconia for energy · Ionic conductivity · Electrical potential generation · Coprecipitation method

## List of Symbols

|                         |   |
|-------------------------|---|
| CPE                     | Constant phase element                      |
| $C^g, C^{gb1}, C^{gb2}$ | Capacity of grain and grain boundary spaces |
| DRS                     | Distribution of relaxation time analysis    |
| $E_a$                   | Energy activation                           |

|           |   |
|-----------|---|
| gb1, gb2  | Grain boundary spaces                         |
| NPs       | Nanoparticles                                 |
| $R$       | Resistor                                      |
| $S_{sa}$  | Specific surface area                         |
| $S_{msa}$ | External and mesoporous specific surface area |
| SEM       | Scanning electron microscopy                  |
| SOFC      | Solid oxide fuel cell                         |
| $T_{cal}$ | Calcined temperature                          |
| $U_{max}$ | Maximum of voltage                            |

✉ Oksana Gorban  
oxanag1@ukr.net

Anton Gorban  
anton.stroncii@gmail.com

<sup>1</sup> Donetsk National Technical University, Pokrovsk, Ukraine

<sup>2</sup> Material Science Department, Donetsk Institute for Physics and Engineering Named After O.O. Galkin NAS of Ukraine, Kiev, Ukraine

<sup>3</sup> REQUIMTE, Faculdade de Ciencias e Tecnologia, Universidade Nova de Lisboa, Quina de Torre, 2829-516 Caparica, Portugal

## 1 Introduction

The strategy of developing the global energy market is based on the advantages of using alternative energy technologies, so-called green ones, over traditional technologies [1]. It is



due to the severe negative impact on the environment of using conventional hydrocarbon energy sources [2]. The technologies of solid oxide fuel cell (SOFC) [3], solar energy [4], humidity to electricity [5] are actively developed. One of the materials used in these technologies is oxide materials with a nonstoichiometric matrix, including zirconia [6]. The nonstoichiometric nature of the material provides high ionic conductivity due to oxygen defects in the volume and at the boundaries of ceramic grains [7], as well as proton conductivity due to the presence of active water adsorption centers on the nanoparticles (NPs) surface [8]. Zirconia has these valuable structural properties, and at the same time, due to its nature, it is a bioinert material, which excludes its toxic effects on the environment. Modern material science uses different synthetic methods to create nanomaterials, for example, plasma chemical technique [9], wet chemistry [10], mechanochemical synthesis [11]. The trend toward decreasing energy intensity of manufacturing makes wet chemistry methods the most promising because of their low cost and the simplicity of synthetic equipment [12]. The coprecipitation method, sol–gel and hydrothermal techniques are the set of wet chemistry methods. In industry, the sol–gel process is used for zirconia synthesis, particularly in Tosoh corporation [13]. However, this method has some limitations. It contains an energy-intensive grinding step [13]. Only NPs with sizes above 40 nm may be obtained [13]. The use of the coprecipitation process gives the more wide possibility for the variation of the properties of synthesized materials, notably decreasing NPs sizes and the variety of the chemical composition of materials due to complex doping in oxide matrix [14]. This method is often used in laboratory practice and pilot production and has good prospects for scaling up to large-tonnage zirconia production. [15]. However, the surface energy of nanoparticles increases significantly, which leads to their aggregation [16]. The NPs aggregation is a negative moment for the successful commercialization of coprecipitation technology since the particle size and dispersity of the material are important characteristics of a commercial product that affect its performance properties along with the chemical and phase composition. At the same time, some parameters of chemical synthesis (nature and concentration of precursor salts and precipitator, pH of a solution, drying and calcined temperature) affect the structural characteristics of the final product [17, 18]. The optimization of material operating properties is achieved by building a correlation between material's functional properties and structure and the characteristics of the initial powder. Thus, for catalysis, oxide particle aggregates can be helpful in the formation of active catalyst clusters in their pores [19], while in technologies using particle ordering during pressing or during slip casting, powder aggregation is undesirable [20]. Technologies for manufacturing critical elements of alternative energy, for example, solid electrolyte, cathode or anode for

SOFC, include techniques for consolidating oxide nanoparticles by pressing or slip casting [21]. Therefore, the successful application of nanopowders in such technologies depends on their dispersity. However, only analysis of the electrophysical properties of materials allows choosing the optimal powder size for such applications. Also, understanding what structural features of the material affect the properties is needed [3, 5].

Materials based on zirconia are widely used in SOFC technology, including solid electrolytes [22]. The level of ionic conductivity determines the functionality of such material. The level of ionic conductivity of zirconia depends on chemical composition [23], the density of materials [24], the type and number of defects in ceramic grains and their boundaries [25, 26]. The use of nanopowders in ceramic manufacturing allows enhancing the functionality of ceramic material [27]. It is known, the size and dispersity of nanopowders are essential characteristics that affect the structure and mechanical properties of ceramic [28]. However, the effect of grain size on bulk and grain boundary ionic conductivity is still under discussion [29–31]. Usually, authors analyze the ionic conductivity of zirconia ceramics with different grain sizes in which grain size is determined by

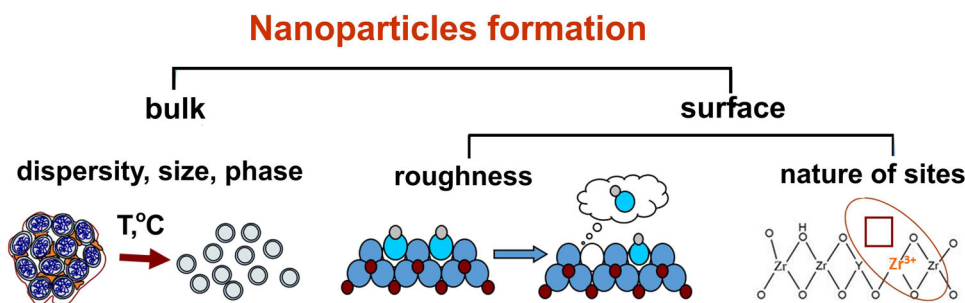
- the sintering temperature of ceramic [22, 30, 32],
- the various kinds and amounts of dopants [22, 29, 30],
- NPs sizes [33, 34].

Analysis of these works indicates discovered links between microstructure (grain sizes), ceramic density and ionic conductivity, but these relationships may not be unambiguous [29, 35]. Since the grain sizes and density are the functions of dopant [33, 34] or sintered temperature [22, 34]. Simultaneous changes in the grain size and density of ceramics formed at different sintering temperatures can lead to an ambiguous interpretation of the relationship between powder characteristics and ceramic functionality. One approach that makes it possible to separately evaluate the contribution of grain size and density of the material to the ionic conductivity is the creation of ceramics with different grain sizes under identical sintering conditions.

This approach realized in works [34, 35] also is not cleaner because NPs with different sizes are usually obtained by the adding of varying dopant amounts [34], mechanical milling [36] or different synthesis routes [37]. It is possible to get ceramics with varying grains at the same sintering temperature using powders with different sizes but synthesized in the same synthetic approach. It will clarify the contributions of grain size and density to the material's functionality.

At the same time, consolidated nanomaterials based on zirconia are promised in new energy generation technologies based on humidity gradient use [10, 38, 39]. For a description of potential electric generation in consolidated nanomaterials

**Fig. 1** Scheme of nanoparticles (NPs) formation of zirconia as smart object



the mechanisms of ion diffusion, surface potential and stream potential are used [40]. The implementation of these mechanisms is based on creating an electrical double layer (EDL) during water adsorption on walls of pores formed between NPs [41, 42]. Materials for this application are subject to the following requirements: NPs dispersity [39], determining surface state [38] and their water adsorption capacity [39, 42]. The latter parameter depends on the dispersity, amounts and nature of active surface centers [43]. At the same time, the sizes, dispersity [44] and surface state [45] of zirconia NPs prepared by coprecipitation technics depend on calcined temperature. In the coprecipitation technology, the zirconia is formed as a smart object because the NPs are characterized by a set of bulk and surface characteristics, Fig. 1. The phase and chemical compositions, type of bulk and surface defects, NPs size, surface state and dispersity index can control by varying reaction conditions.

For successful commercialization of chemical coprecipitation process in the actively developing sector of alternative energy technologies, a qualitatively new procedure for work organizing in a scientific laboratory of nanomaterials is required. The order is based on the approach of task-oriented engineering of nanomaterials which is applied for broad spectra of application, for example, membrane design [46], catalysts [19, 47], optics in solar devices [48], sensors [4].

The NPs chemical engineering is based on bonds: “materials characteristics—operated or functional properties of NPs—functional properties of ceramic material”. In this case, the interaction between the researchers, who synthesizes and tests material structural and functional properties, must be thoroughly organized. It requires the building of optimal workflows in a laboratory of nanomaterials.

For optimization of work in laboratory of nanomaterials needs:

1. to build an algorithm of synthesis based on the choice of critical parameters effected on material structure;
2. to select methods of study that allow describing the structure and functional properties of the material;
3. to determine workflows that provide the optimal performance of the necessary research procedures for building

“materials structure—material functionality” correlation.

It may be realized in SmartLab conception widely developed recently [15, 49].

The aim of work was

- the development of SmartLaboratory concept that allows providing the choice of key criteria for the synthesis of high dispersed zirconia nanopowders with predetermined sizes by coprecipitation method;
- the production of ceramic materials with different grains size in identical thermodynamic conditions (1350 °C) based on NPs with variance size;
- the study of the impacts of grain size and density of powder compact and ceramic on electrophysical properties of zirconia for subsequent development of coprecipitation technology for task-oriented production of nanosized zirconia for alternative technology.

## 2 Materials and Methods

### 2.1 Materials

ZrOCl<sub>2</sub>·6H<sub>2</sub>O was obtained from SME “CVK” (Ukraine) and Y(NO<sub>3</sub>)<sub>3</sub> was prepared by dissolving of commercial Y<sub>2</sub>O<sub>3</sub> (GAS 1314-36-9) in 65 wt% HNO<sub>3</sub> (GAS 7697-3-2). Ammonia 25 wt% water solution was used. All reagents was used without further purification.

### 2.2 Synthesis of Zirconia NPs

Y-doped zirconia nanopowders or materials were synthesized by inverted coprecipitation method. ZrOCl<sub>2</sub>·6H<sub>2</sub>O and Y(NO<sub>3</sub>)<sub>3</sub> in same stoichiometry mole ratio of yttrium and zirconium oxides—3:97 are used. The concentration of zirconium salt is varied in a range of 0.39–2.33 mol/L. Ammonia solution was employed to precipitate the zirconium hydroxide hydrogel. The precipitation process was carried out at

the solution pH = 9–10. Hydrogel precipitate was repeatedly washed by distilled water to pH = 7–8. The absence of Cl<sup>-</sup> ions in wastewater was checked also. MW oven is used to dry hydrated zirconium hydroxide ( $f = 2.45$  GHz,  $P = 900$  W). The calcination of the dried zirconium hydroxide occurs during isothermal treatment ( $T_{cal}$ ) at 400–1000 °C for 2 h.

## 2.3 Consolidated Powders and Ceramic Samples Preparation

Zirconia NPs compacts (20 mm in diameter) were produced by uniaxial pressing of zirconia powders in metallic die at 30 MPa and then cold isostatic pressing (CIP) in an oil (VG 32) at 300 MPa. The ceramic sample is prepared from zirconia NPs compacts by heat-treatment at the sintered temperature of 1350 °C for 2 h.

## 2.4 Characterization

### 2.4.1 X-Ray Diffraction Measurement

XRD patterns are obtained in filtered (Ni filter) CuK $\alpha$ -irradiation ( $\lambda = 1.54$  Å) on powder diffractometer Dron-3, Bourestnik, Russia. For tetragonal and monoclinic phases of zirconia, the analyzed space groups were P42/nmc and P21/C, according to the ICDD standard card N01-078–1765 and 0–037-1484, accordingly. Selyakov-Sherrer's equation was used for estimation the coherent scattering area (CSA) of powder samples. The estimation error of particle size is 1 nm.

### 2.4.2 Textural Measurement

Nitrogen adsorption–desorption isotherms at 77 K is measured on SORBI MS 4 N device at N<sub>2</sub> + He mix partial pressure ( $p/p_0 = 0.05 \div 0.95$ ). Preliminary heat treatment of powder samples occurs at 140 °C for 30 min for adsorbed water removal. Values of specific surface area ( $S_{sa}$ ) and specific surface area of mesopores ( $S_{msa}$ ) are estimated in the SoftSorbi-II v. 1.0 program. For the description of specific surface area ( $S_{sa}$ ) the adsorption isotherm in range  $p/p_0 = 0.06–0.2$  was used according to BET method [50]

$$\frac{P/P_0}{V_a(1 - P/P_0)} = \frac{1}{V_m C} + \frac{C - 1}{V_m C} \frac{P}{P_0}, \quad (1)$$

where  $V_a$  is volume of adsorbed gas;  $V_m$ —monomolecular layer volume;  $C$ —BET constant,  $p$ —equilibrium gas pressure;  $p_0$ —partial pressure and specific surface area ( $S_{sa}$ ) is

$$S_{sa} = 4.371 \cdot V_m. \quad (2)$$

$S_{sa}$  value includes the external, mesopores and micropores specific surfaces area. The measurement error is not more than 3%.

The external and mesopores specific surface area ( $S_{msa}$ ) and micropores volume ( $V_{micro}$ ) is estimated by t-method (STSA) [51]. The adsorption isotherm is analyzed at  $p/p_0 = 0.39–0.53$ . Pore geometry is cylindrical.  $S_{msa}$  was estimated from adsorption isotherm in coordinates  $V_a-t$  (STSA-graph), where  $t$  is medium thickness of adsorbed layer estimated by the Halsey equation

$$t = 3.54 \cdot \left( \frac{5}{2.303 \cdot \log\left(\frac{P_0}{P}\right)} \right). \quad (3)$$

Then,  $S_{msa}$  is estimated from linearization isotherm as:

$$S_{msa} = \left( \frac{V_a \cdot 15.47}{t} \right) \quad (4)$$

The measurement error is not more than 3%.

### 2.4.3 TEM, SEM Investigation

Morphology of powder is determined by transmission electron microscopy (TEM) using JEOL JEM 200A microscope. The morphologies of consolidated powder and ceramic are determined by transmission electron microscopy (SEM) using JSM 6490LV JEOL Japan. The grain size estimation is provided by a method of random section medium values.

### 2.4.4 pH Meter Measurement

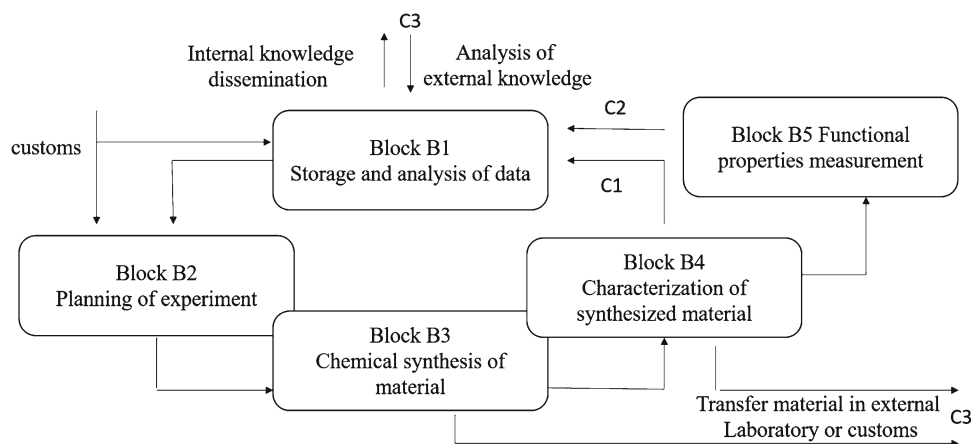
The integral acidity of oxide NPs surface and analysis of air-drying and water-saturated states is determined from pH measurement (“pH 700” pH meter, Eutech Instruments, Singapore) [52]. The  $\xi$ -potential of NPs obtained from the analysis of electroosmosis data [53]

$$\xi = \frac{\eta}{\varepsilon \cdot \varepsilon_0} \cdot \frac{U_o^V \cdot K_x}{I} \quad (5)$$

where  $\eta = 1 \times 10^{-3}$  (N s/m<sup>2</sup>) is viscosity of water media;  $\varepsilon = 81$ —dielectric constant of water;  $\varepsilon_0 = 8.85 \times 10^{-12}$ —the vacuum permittivity (F/m);  $U_o^V = V/t$ —volume rate of solution at electroosmosis (m<sup>3</sup>/s);  $K_x = K_{KCl} \cdot (R_{KCl}/R_x)$ —specific electroconductivity of medium, ( $1/(\Omega \text{ mm})$ ),  $R_{KCl}$ —resistance of 0.01 mol/kg KCl solution;  $R_x$ —resistance of filtrate.  $I$ —current (A).  $\xi$ -zeta potential value of NPs is estimated as average of values from three measurements.



**Fig. 2** Scheme of main stages of management of working process in chemical laboratory



#### 2.4.5 Impedance Measurements

The impedance of ceramic was measured by virtual precision analyzer of impedance parametrizes 2B-1 (Trapeznicov Institute, Russia) in frequencies of 1 Hz–3 MHz and temperature from 210–910 °C range. The points in the frequency range of 0.1 Hz–3 MHz were 52. In order to ensure the linearity of the studied electrochemical system, the amplitude of the variable excitation signal applied to the sample was limited to 50 mV. The impedance spectra in terms of distribution of relaxation times (DRT analysis) obtained in Program RelaxIS 3 (RHD instruments GmbH & Co. KG, Germany) [54, 55]. Samples for measuring the temperature dependence of the impedance had the shape of a disk with a diameter of  $10.0 \pm 0.5$  mm and a thickness of  $2.00 \pm 0.05$  mm. To create reliable electrical contacts on the end surface of the samples was applied a thin layer of silver paste (40–50  $\mu\text{m}$  thick), which was ignited at a temperature of 910 °C for 30 min. Platinum wires were pressed to the formed metallic silver contacts on the ceramic sample, which were connected to the input terminals of the impedance analyzer. The total grain and grain boundary conductivities ( $\sigma$ ) are estimated as [56, 57]

$$\sigma = \frac{L}{RS}, \quad (6)$$

where  $L$ —sample thickness and  $S$ —electrodes surface,  $R$ —resistivity of material.

For registration of maximum of voltage ( $U_{\text{max}}$ ) in pressed powders samples ( $m = 2$  g), the precision voltmeter Kethly 2000 was used. Graphite was used as an electrode on the side of pressed powders samples.

#### 2.4.6 Density Measurement

Densities of pressed compact and ceramic samples are estimated by hydrostatic weighing according to GOST 15,139–69.

#### 2.5 Procedures of Decomposition Diagram

The working process in a laboratory of nanomaterials synthesis is described based on the method of decomposition diagram [58]. The decomposition diagram allowed us to select the kinds of works and links between separate worked stages, define the work tasks, choose objects, and determine workflows in laboratory.

### 3 Results and Discussion

#### 3.1 Structure of Laboratory of Nanomaterials

In a SmartLab conception, the architecture of a laboratory is selected based on the features of chemical engineering of nanomaterials [49]. For the research laboratory of functional nanomaterials, the working process is multilevel and may contain reversible cycles between different levels.

Figure 2 shows a scheme of the central management stages of the chemical laboratory's working process. According to the presented information, the main workflows in the Laboratory of nanomaterials link the following main blocks:

1. Block B1—Storage and analysis of data;
2. Block B2—Planning of experiment;
3. Block B3—Chemical synthesis of material;
4. Block B4—Characterization of synthesized material;
5. Block B5—Functional properties measurement.

The distribution of workflows can be described by two inner closed cycles (small cycle C1 and big cycle C2) of workflows and outer workflows directly related to other laboratories, databases, and open scientific space (conference, articles, different types of dissemination). The outer workflows are included in external cycle C3. The last determines the transfer materials or some results from Block B2, Block B3, or Block B4 to external laboratories for study materials

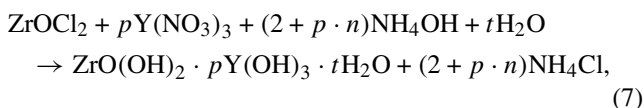
or data process and return the data and results from outside to Block B1. The computerization of such laboratory should provide the full support of all operations. These operations are necessary calculations, the work with database and data storage, visualization, analysis program, chemical process control automation, sensors, others, and the creation and support of a fast exchange of information inside marked Blocks.

Chemical engineering of nanomaterials occurs in technological processes of synthesis. According to created synthesis protocol in Block B2, the chemical synthesis carries out in Block B3. Block B3 is a central block in laboratory. Block B3 has a hardware-software blocks solution for equipment starts and synthesis controls. Block B3 structure is described through the set of hardware and software subsystems. The synthesized materials transfer to Block B4 and Block B5 for characterization and testing. The obtained data is used for technological process optimization.

### 3.2 Choice of Key Parameters for Technological Process Optimization

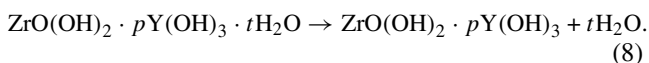
The technological process of obtaining crystalline zirconia may be described in detail as:

*1st stage* The forming of a wet hydrogel of Y-doped zirconium hydroxide by chemical coprecipitation method [59] according to the following reactions:



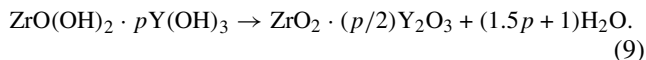
Y—doping element,  $n$ —valence of Y,  $p$ —Y amount (mol%) according to the ratio between Zr and Y in oxide,  $\text{ZrOCl}_2$ ,  $\text{Y}(\text{NO}_3)_3$ —zirconium and yttrium salts,  $\text{NH}_4\text{OH}$ —precipitator. The amount of Y-doped zirconium hydroxide hydrogel obtained from zirconium salt depends on its concentration.

*2nd stage* The forming of amorphous Y-doped zirconium hydroxide (xerogel) occurs using high energy MW irradiation ( $f = 2.45$ ,  $P = 700\text{--}900$  W) from the hydrogel. In such drying, the system lost some part of free and physical adsorbed water [60]. The scheme of xerogel formation may be expressed as:



Synthesized amorphous product contains some chemical linked water. There are terminal and bridging OH groups [61]. Their ratio determines the degree of connection of NPs each to the other in xerogel. The degree of NPs aggregation in the amorphous xerogel matrix determines the dispersivity of synthesized oxide particles [62].

*3rd stage* Oxide NPs is formed by isothermal heat treatment of amorphous xerogel at temperature from 400 to 1000 °C range according to scheme:



The size of the crystalline particle is regulated at this stage [44].

Usually, the conditions of the first and second stages determine the dispersivity of crystalline zirconia. The sequence of steps proposes the influence of each key parameter from the previous step on the structures and properties formed product. In connection with it, some correlations between key parameters of synthesis and structure, functionality created product are needed. The critical structure parameters influence on optimal characteristics of obtained products.

The zirconium salt concentration is a critical technological parameter in the first technological stage, according to (7). It is due to two opposite factors, namely, on the one hand, a decrease in the salt concentration improves the dispersion of the material [59, 63], and on the other hand, it reduces the yield of the target product [15]. The choice of optimal salt concentration is essential for the dispersivity of oxide products with optimal target product yield. In the second stage (8), the drying intensity is a primary technological parameter, and the use of high energy methods, such as microwave irradiation, can improve material dispersivity [59]. In the third stage (9), oxide nanoparticles are formed under isothermal heat treatment, and their sizes are the function of calcined temperature [44, 63].

Thus, the zirconium salt concentration and calcined temperature may be chosen as technological parameters of coprecipitation method for obtaining materials with predetermined particle sizes and dispersivity.

#### 3.2.1 Correlation of “Key Parameter of Synthesis: Key Structure Criterion

**Calibration I: “Salt Concentration—Powder Dispersivity”** The calibration of “key parameter of synthesis—key structure criterion” must be built to determine the optimal salt concentration. The zirconium salt concentration is a key parameter of synthesis. The dispersivity of amorphous zirconium hydroxide is the key structure criterion.

The ratio terminal and bridging OH groups, specific surface area and micropores volume, the fractal dimension of oxide systems estimated by FTIR spectroscopy [45], BET analysis [48, 51, 62] SANS or SAXS methods [45, 61, 62], accordingly, may be used for the description of the aggregation index of oxide powders. Any of the characteristics may be used as a key structure criterion of material. Still, investigators often choose the specific surface area value to estimate

**Table 1** BET data for xerogel synthesized from salt solution of different concentration

| $C$ (mole/L) | $S_{sa}$ | $S_{msa}$ | $S_{msa}/S_{sa}$ | $V_{micro}$ | System type         |
|--------------|----------|-----------|------------------|-------------|---------------------|
| 0.39         | 368.4    | 369.5     | 1                | 0.0         | Meso structure      |
| 0.78         | 379.3    | 381.6     | 1                | 0.0         | Meso structure      |
| 1.16         | 343.4    | 282.7     | 0.8              | 0.022       | Micromeso structure |
| 1.51         | 316.6    | 234.1     | 0.7              | 0.033       | Micromeso structure |
| 2.33         | 313.2    | 201.7     | 0.6              | 0.047       | Micromeso structure |

The error for  $S_{sa}$ ,  $S_{msa}$  estimation is 6%

powder dispersity and aggregation index for the broad spectra of materials [48, 51, 64]. The NanoDefine project ([www.nanodefine.eu](http://www.nanodefine.eu)) proposed the flow chart of the nanomaterials and non-nanomaterials screening strategy based on BET measurement and the subsequent confirmation of material's dispersity by electron microscopy [65].

Table 1 shows BET data for xerogel synthesized from salt solutions with different concentrations, including specific surface area estimated by BET ( $S_{sa}$ ) and  $t$ -method ( $S_{msa}$ ) approaches and micropores volume ( $V_{micro}$ ) according (1)–(2) and (3)–(4).

It was found, that the specific surface area ( $S_{sa}$ ) of amorphous xerogel depends nonmonotonically on salt concentration taken during powder synthesis. It may be due to the difference in porous structures of formed xerogels. In this case the value of  $S_{msa}$  estimated by  $t$ -method (3)–(4) is needed using additionally to  $S_{sa}$  value [64], since  $S_{sa}$  estimated by BET method (1)–(2) cannot separate the pore surface from external surface area of NPs [65]. According to [66], the ratio of  $S_{sa}/S_{msa}$  reflects the degree of mesoporosity versus microporosity in investigated materials. The xerogels are mesoporous systems if  $S_{msa}/S_{sa} \geq 1$ , but the xerogels are micromesoporous systems if  $S_{msa}/S_{sa} < 1$ . Thus, the  $S_{msa}/S_{sa}$  ratio may be used as criterion for a description of the amorphous xerogel structure. The aggregation index of the oxide system depends on the porous structure of using amorphous xerogel [10, 62]. TEM investigation of formed oxide NPs allows visualizing the NPs aggregation index. Figure 3 shows TEM data of oxide powders (700 °C) obtained from mesoporous (Fig. 3a) and micromesoporous xerogels (Fig. 3b). The oxide powders synthesized from mesoporous xerogel contain the aggregates of soft linked NPs. The oxide system synthesized from micromesoporous shows the presence of hard aggregates in powder structure. It was shown in [61, 62] for zirconia the transfer from mesoporous to micromesoporous structure increases the number of phase contacts between amorphous NPs due to increasing of bridging OH-groups in its structure. The process of the oxolation of such groups during heat treatment of xerogel leads creating the hard linked oxide NPs. Thus, the using of mesoporous xerogel allows preparing the dispersive oxide systems.

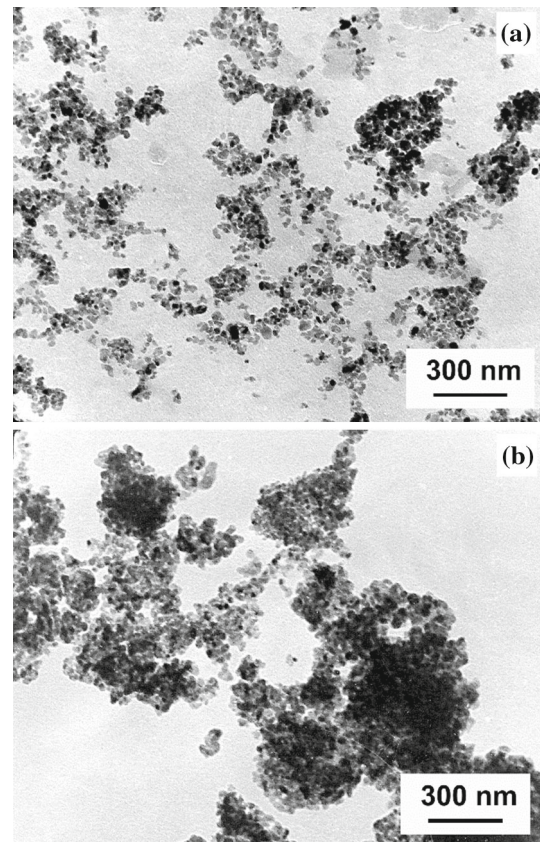


**Fig. 3** TEM data of oxide powders (700 °C) synthesized from **a** mesoporous and **b** micromesoporous xerogels

It is concluded that the absence of micropores in the initial amorphous xerogel is a quantitative criterion for the dispersion of oxide NPs. The  $S_{msa}/S_{sa}$  ratio estimated for the amorphous xerogel can be used as a qualitative criterion for the fineness of the resulting oxide powders. The TEM data shows that synthesized oxide is dispersive if the  $S_{msa}/S_{sa} = 1$  is fulfilled. Critical salt concentration solution used for zirconia precipitation process must be less than 1 mol/L.

Figure 4 presents the flow chart for the building of the calibration I of “zirconium salt concentration—powder dispersity” ( $S_{msa}/S_{sa} \geq 1$  for amorphous xerogel is satisfied condition) in terms of “key parameters of synthesis—key structure criterion”.

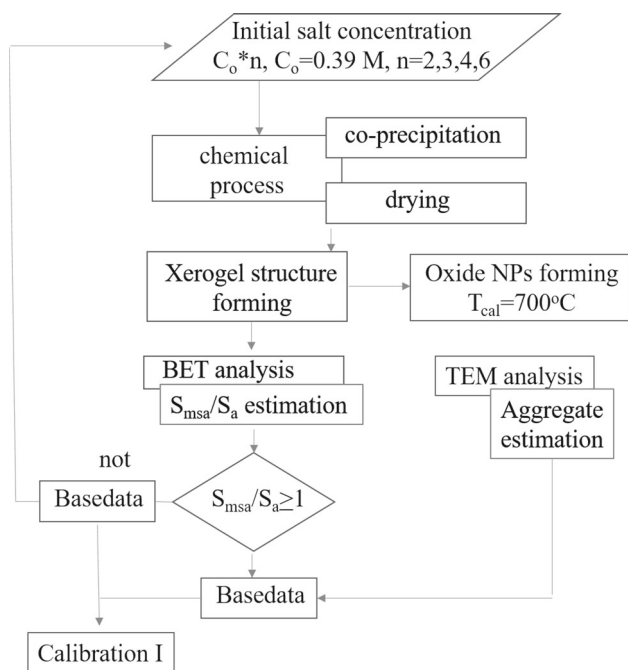


**Fig. 4** The algorithm of building calibration I of “zirconium salt concentration—dispersity of xerogel ( $S_{msa}/S_{sa}$ )”

Flow chart (Fig. 4) contains some procedures:

1. The synthesis of amorphous xerogel correspond to (7)–(8) from solutions with different salt concentrations. Zirconium salt concentration is varied from 0.39 to 2.33 mol/L with a step of 0.39.
2. The calculation of  $S_{sa}$  and  $S_{sma}$  values for amorphous xerogel based on BET data according to (1)–(2) and (3)–(4). The check of  $S_{msa}/S_{sa}$  ratio.
  - if  $S_{msa}/S_{sa} \geq 1$ , structure classifies as mesoporous;
  - if  $S_{msa}/S_{sa} < 1$  structure classifies as microporous.
3. The synthesis oxide NPs by isothermal treatment at 700 °C according to (9). The estimation of aggregation index for oxide NPs by TEM investigation.
  - if xerogel is mesoporous system then oxide NPs will dispersive;
  - if xerogel is microporous system then oxide will not dispersive.
4. The building of the calibration I: “salt concentration—oxide dispersive” (Table 1) Data is saved in Basedata.

Calibration I allows to choice concentration of zirconium salt that is optimal for synthesis of mesoporous xerogel. It allows obtaining the high dispersed oxide product in future.

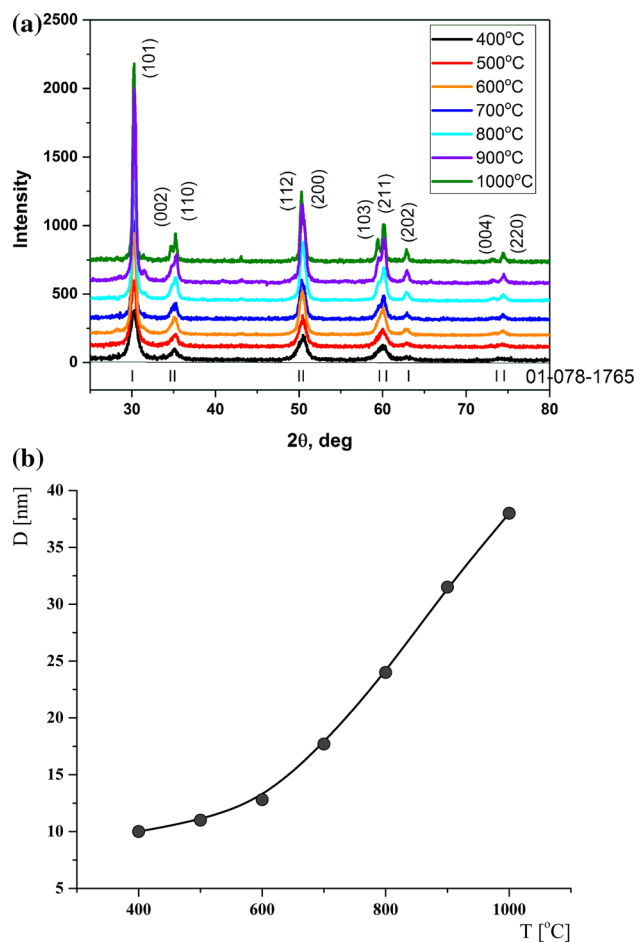


**Fig. 5** XRD analysis **a** XRD pattern, **b** The calibration II of “calcination temperature—NPs size” for 3 mol% Y-doped zirconia.  $D$  is NPs size,  $T_{cal}$ —calcined temperature. 01-078-1765 is card number in ICDD database

#### Calibration II: “Calcined Temperature:Nanoparticles Size”

Oxide NPs are synthesized according to (9). All synthesized zirconia systems are tetragonal crystals. Figure 5a shows the XRD pattern. The observed X-ray reflections exhibit a good agreement with the ICDD standard card 01-078-1765 for P42/nmc. Doping of zirconia lattice by  $Y^{3+}$  ions led to stabilize tetragonal phase according to  $ZrO_2$ - $Y_2O_3$  phase diagram [14]. For oxide systems, the increase of calcined temperature ( $T_{cal}$ ) leads to an increase in the size of synthesized NPs [44]. However, NPs growth at increasing the calcined temperature depends on the nature of oxide matrix, kinds and concentration of dopant, and isothermal treatment time [67]. Figure 5b shows the dependence of NPs size on calcined temperature for Y-doped zirconia synthesized from solution with zirconium precursor salt concentration 0.78 mol/L.

The curve shows the monotonic growth of NPs sizes at increasing of  $T_{cal}$ , and it may be described as exponent trend ( $R^2 = 0.9917$ )

$$D = 1.27 \cdot \exp(0.0027 \cdot T), \quad (10)$$



where  $T$ —temperature in K. For Y-doped zirconia the NPs size increases 3.5 times with increasing of  $T_{\text{cal}}$  from 400 to 1000 °C.  $D$  at  $T = 298$  K is the size of an amorphous particle of xerogel.

Thus, these two selected correlations allow writing the synthesis protocol of dispersive Y-doped zirconia NPs with predetermined sizes.

### 3.3 Functionality of Nanosized Material in Energy Application

The electro-physical properties of pressed powders and sintered ceramic systems obtained from NPs with different sizes were tested to estimate the functionality of synthesized zirconia for energy applications. The ionic conductivity of ceramic samples and the ability of powders compacts to generate the electric potential in a humid atmosphere versus  $T_{\text{cal}}$  of powders were estimated. The ceramic samples sintered at 1350 °C were tested by impedance spectroscopy for the ionic conductivity experiments. The electric potential were tested at 80% air humidity for compacted powder samples.

#### 3.3.1 Dependence of Compacts and Ceramic Properties from Nanopowder Sizes

As taken above, the powders pressed by CIP and ceramic samples are used for testing. The density is a main physical characteristic of these samples [22, 24, 29]. Figure 6a shows the density of pressed powder and sintered ceramic samples from powders with various calcined temperatures (in other words—NPs sizes). This dependence is non-monotonic with extremum at 700–800 °C corresponding to NPs sizes—18–24 nm. It correlates with the changing the NPs  $\xi$ -potential from  $T_{\text{cal}}$  of NPs, see Fig. 6b. The values of  $\xi$ -potential for oxide NPs connect with surface state [68]. The relation of the number of basic and acidic sites (Lewis and Bronstad) determines the acid–base state of NPs surface [42]. According to (8)–(9), oxide NPs are formed due to the dehydration and dehydroxylation of amorphous xerogels at heat treatment. It leads forming of Lewis acid sites (oxygen vacancies) on zirconia surface at low annealing temperatures [45]. The calcination of NPs in atmospheric oxygen increases the Lewis basic sites on surface (surface oxygen), resulting in the ratio of acidic and basic sites changes [43, 45]. The extremum on this dependence shows on changing of nature of surface sites.

It is known that  $\xi$ -potential influences on NPs aggregation and disaggregation [68]. Additionally, the frame structures in pressed samples are created by aggregates present in powders with  $T_{\text{cal}} = 1000$  °C. They give an additional part in the decreasing of density, Figs. 6a and 7 show the changing of ceramic structure for nanopowders with different  $T_{\text{cal}}$ .

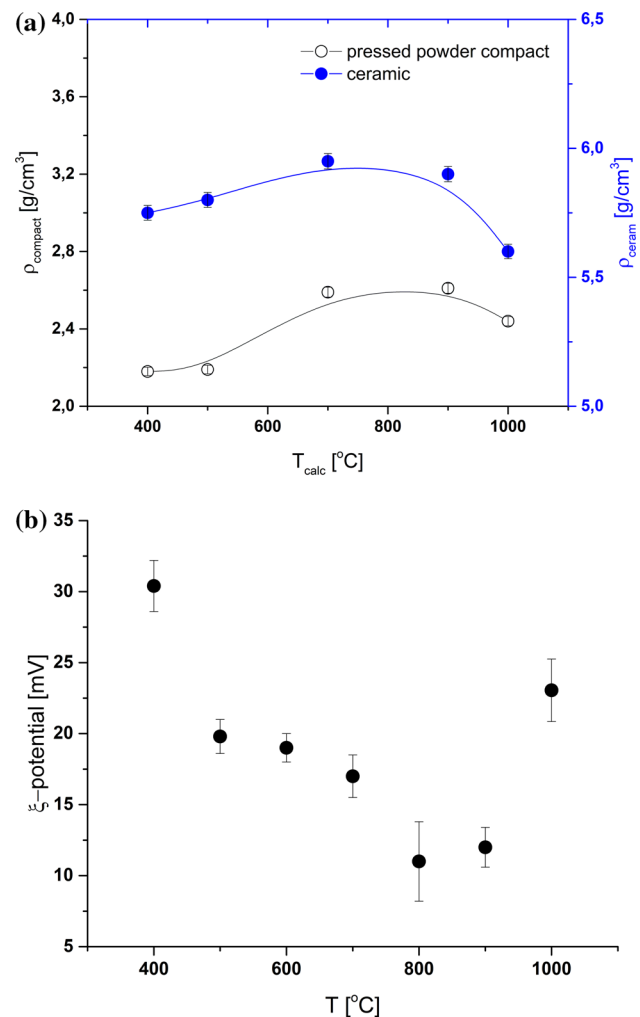


**Fig. 6** Characteristics of powders versus  $T_{\text{cal}}$  of powders **a** densities of pressed powder ( $\rho_{\text{compact}}$ ) and sintered ceramic samples ( $\rho_{\text{ceramic}}$ ), **b**  $\xi$ -potential of NPs

The values of average grain sizes of Y-doped ZrO<sub>2</sub> ceramics are  $176 \pm 23$ ,  $202 \pm 19$ ,  $214 \pm 13$ ,  $239 \pm 21$ ,  $290 \pm 33$  and  $340 \pm 23$  nm for ceramic sintered from NPs obtained at 400, 500, 700, 800, 900 and 1000 °C. In this case, the ceramic grain size and density are functions of NPs sizes (or  $T_{\text{cal}}$ ) taken on for ceramic synthesis. It contrasts with other works in which grain size and density are functions of ceramic sintering temperature [25]. It helps to separate the influence of grain size and density on zirconia's electrophysical properties and optimize the characteristics of zirconia powders proposed for energy application.

#### 3.3.2 Ionic Conductivity of Y-Doped Zirconia Ceramic from NPs with Different Sizes

The impedance spectroscopy allows to dilute the ionic and electronic parts in total conductivity in the ionic solid electrolyte, the inner and inter grains conductivity in crystalline

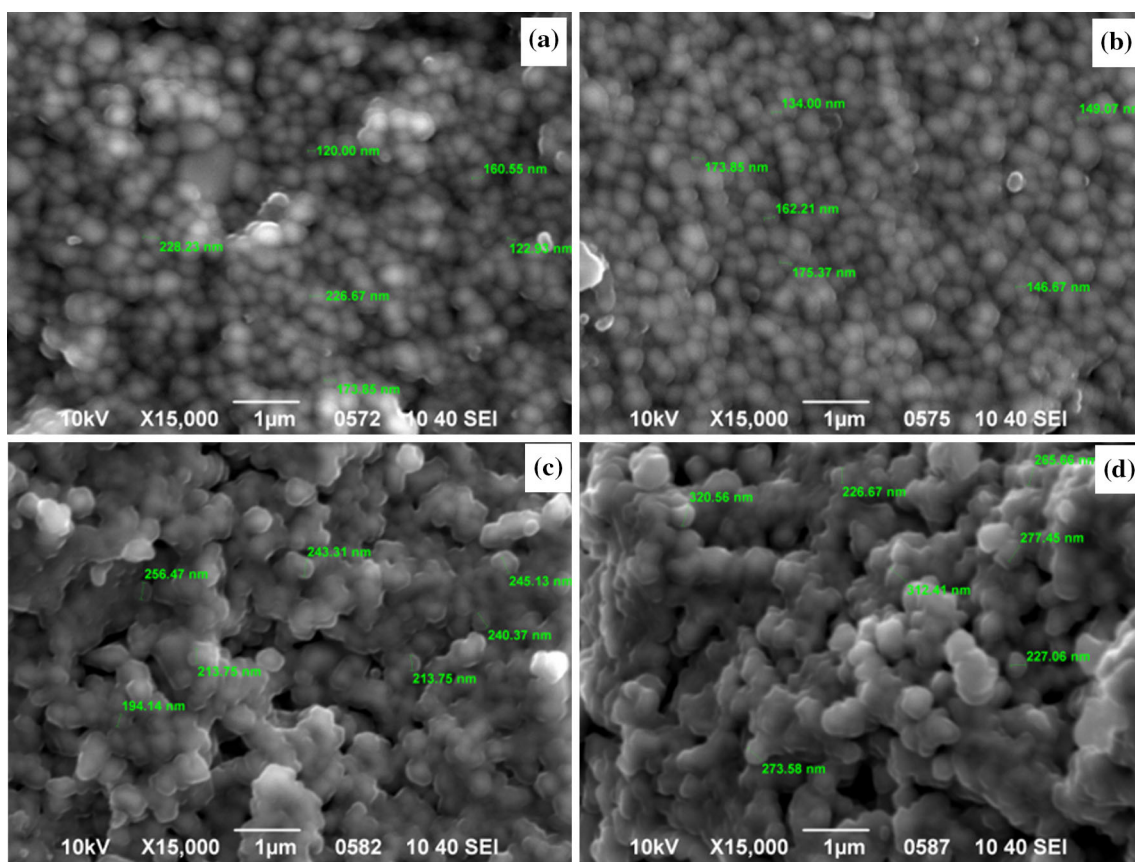


**Fig. 7** SEM images of ceramic structure synthesized at 1350 °C from NPs with  $T_{cal}$ —**a** 500 °C, **b** 700 °C, **c** 900 °C and **d** 1000 °C

materials. Figure 8 shows impedance spectrum pattern which is typical for this type of materials [29, 69]. It contains one or more semicircles, overlapping or not, which describe the contributions of volume (grains), interfaces (mainly grain boundaries), and contacts to the electrical resistivity of polycrystalline ceramics [56]. Sometimes, in the low-frequency part of impedance spectrum, the straight line may be observed and it is attributed to Warburg impedance connected with ion diffusion [70]. Each semicircle is represented by an equivalent circuit composed of a resistor (R) in parallel with a constant phase element (CPE) when the centers of these semicircles lie below the ReZ axis [71, 72]. The CPE is mathematically generalized from the capacitor, resistor, and inductor elements according to electrical circuit theory [73]. The impedance of a CPE is given by

$$\text{CPE} = \frac{1}{Q(i2f)^\alpha} \quad (11)$$

where  $Q$  is the CPE parameter ( $F \text{ cm}^{-2} \text{ s}^{\alpha-1}$ ),  $i$ —the unit imaginary number,  $f$ —the frequency ( $\text{rad s}^{-1}$ ), and  $\alpha$  is exponent number ( $0 < \alpha < 1$ ) [72, 73]. CPE describes the ideal capacitor with capacitance ( $Q$ ) when  $\alpha = 1$  [72]. The CPE is non-ideal capacitor at fitting impedance data by  $\alpha = 0.8$ – $0.95$

[73]. In this case, the physical meaning of  $\alpha$  is ambiguous connected with non-ideality of the device [74].

The high-frequency semicircle is an attribute of the electrical response of the bulk of the polycrystalline specimen. The low-frequency semicircle is assumed to represent the electrical properties of the highly resistive grain boundaries [75]. The lowest frequency semicircle corresponds to the phenomena at the contacts of the sample. Analysis of impedance spectra allows estimating the bulk and grain boundary specific conductivity ( $\sigma$ ), specific resistance ( $\rho$ ) and activation energy ( $E_a$ ) of ionic conductivity for ceramic obtained from NPs with various calcined temperatures.

It is known that ionic conductivity is determined by oxygen diffusion in zirconia, which depends on temperature measurements ( $T_m$ ). Figure 8a shows impedance spectra in the [ImZ vs ReZ] impedance diagrams, and Fig. 8b shows the impedance spectra in terms of distribution of relaxation times (DRT analysis) obtained in Program RelaxIS 3 [54, 55]. These patterns demonstrated the impedance data for ceramics obtained from NPs of different sizes; spectra are measured at 420 °C. The experimental grain resistance ( $R_g$ ) and grain boundary resistances ( $R_{gb1}$ ,  $R_{gb2}$ ) is calculated from the semicircular arcs in impedance spectra. According to DRT analysis, four processes with different relaxation

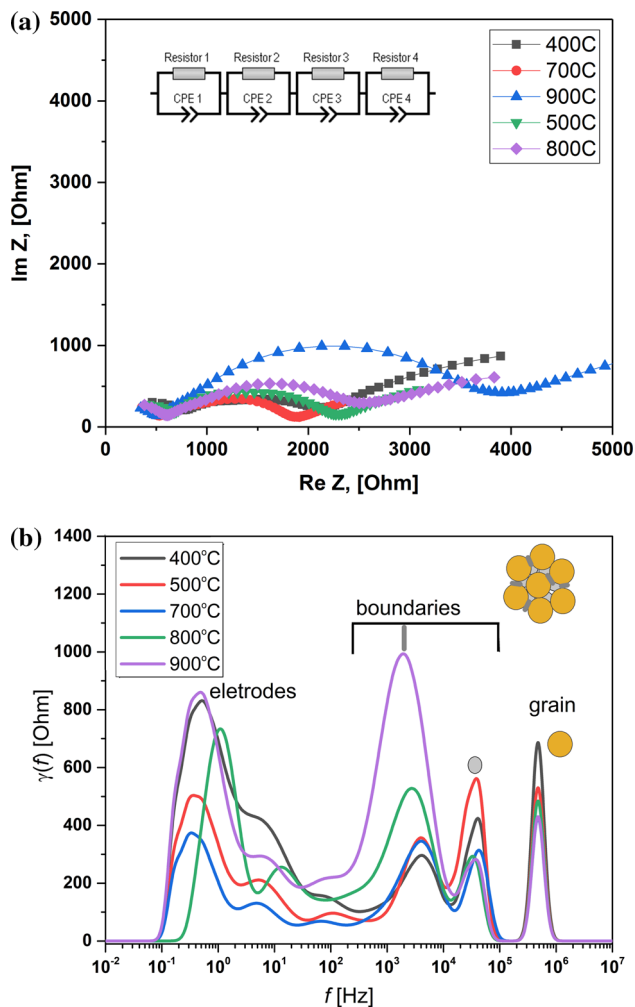


**Fig. 8** The impedance spectra **a** in the [ImZ vs ReZ] impedance diagrams, **b** in terms of distribution of relaxation times (DRT analysis).  $f$ —frequency,  $\gamma(f)$ —intensity signal

times may be selected in DRT spectra. Values of relaxation time and corresponding frequencies of these processes are displayed in Table 2.

The process with maximal relaxation time ( $\tau^{el}$ ) 0.34 s ( $f = 0.47$  Hz) corresponds to electrode polarization [76]. In the equivalent scheme it is marked as electrode resistance ( $R_e$ ) with CPE4 (inset in Fig. 8b). The process with minimal relaxation time ( $\tau^g$ ) of  $3.34 \times 10^{-7}$  s (high frequency—0.47 MHz) corresponds to the process that occurred in bulk [55]. For all investigated systems, this relaxation time is the same. It is evidence of the identical internal structure of formed grains from NPs of different sizes. In equivalent scheme it is described as bulk resistance ( $R_g$ ) with CPE1, inset in Fig. 8b. Two processes in the medium range with relaxation times ( $\tau^{gb1}$  and  $\tau^{gb2}$ ) may be linked with the grain boundaries of different geometries. In equivalent scheme they are described as grainboundary resistances ( $R_{gb1}$ ,  $R_{gb2}$ ) with CPE2 and CPE3 (inset in Fig. 8b). For ceramics sintered from NPs with  $T_{calc}$

above 700 °C, the values of  $\tau^{gb1}$  and  $\tau^{gb2}$  are shifted to the side of low frequencies compared with ceramic from NPs with  $T_{calc}$  of 400–700 °C. The intensities of peaks on DRT curves at  $\tau^{gb1}$  and  $\tau^{gb2}$  are changing opposite at increasing grains in ceramic. The estimated capacities values for these elements of the equivalent electrical scheme (Table 2) show a higher value for gb2 element than for gb1. The order of their capacities indicates the different sizes of such grain boundary spaces [77]. The analysis of  $C^{gb1}$  and  $C^{gb2}$  values shows that the gb1 space is thicker than gb2 space. The grain capacity regularly decreases with a grain increasing because the  $w/d_g$  is still less than 1 and parameter  $d_g$  plays a significant  $C^g$  part. Here,  $w$  is the diameter of grain-to-grain contact, and  $d_g$  is grain diameter.

Additional parameters were calculated to clarify the features of gb1 and gb2 spaces. The blocking factor ( $\alpha_R$ ) and frequency factor ( $\alpha_f$ ) are estimated as [78]

$$\alpha_R = \frac{R^{gb}}{(R^g + R^{gb})}, \tag{11}$$

$$\alpha_f = \frac{f_0^{gb}}{f_0^g}, \tag{12}$$

where the  $R^{gb}$ ,  $R^g$ —resistances of grain boundary and grain spaces,  $f_0^{gb}$ ,  $f_0^g$ —grain boundary and grain semicircle relaxation frequencies.

The geometric correction factors ( $f_{geo}$ ) and diameters of grain-to-grain contact area ( $w$ ) are calculated based on a method to [79]

$$\frac{R^{gb}}{R^g} = f_{geo} \frac{d_g}{w}, \tag{13}$$

$$f_{geo} = \frac{1 - w/d_g}{1 + w/(2 \cdot d_g)}, \tag{14}$$

The values of  $\alpha_R$ ,  $\alpha_f$  are presented in Table 2. It is known, the  $\alpha_f$  is proportional constant to the thickness of grain boundary and  $\alpha_R \approx$  grain boundary area. It allows estimating the grain boundary volume by multiplying them, according to [69, 78]. Together with capacity values, these two independence parameters show different gb1 and gb2 spaces for all investigated systems and predicate bigger size for gb1 space. It is noted that  $\alpha_f^{gb1}$  does not depend on grain size, but the  $\alpha_R^{gb1}$  shows some growth for ceramics with grains of 200–220 nm (NPs with  $T_{cal} = 500$ –700 °C). Last has a higher density than ceramics with smaller and bigger grains. The  $\alpha_f^{gb2}$  does not show growth for ceramic with grain size less 220 nm, but for ceramic with grain sizes > 220 nm, it decreases. Parameter of  $\alpha_R^{gb2}$  is increasing at grain size growth that demonstrated on change geometry of gb2 space due to the increase in the diameters of grain-to-grain contact ( $w$ ) and some pores for

**Table 2** Parameters of grain (g), and two grain boundary (gb1, gb2) spaces

| Range | Parameters  | $T_{\text{calc}}$ of NPs taken on synthesis ceramic at 1350 °C |        |        |        |        |
|-------|---|--|--------|--------|--------|--------|
|       |   | 400 °C   | 500 °C | 700 °C | 800 °C | 900 °C |
| g     | $d_g$ (nm)  | 176  | 202    | 214    | 239    | 290    |
|       | $R^g$ (Ohm <sup>-1</sup> m <sup>-1</sup> )            | 780  | 676    | 502    | 575    | 475    |
|       | $C^g$ (nF)  | 1.21   | 0.52   | 0.14   | 0.21   | 0.18   |
|       | $w$ (nm)  | 70.8   | 63.5   | 77.4   | 111    | 97.5   |
| gb1   | $\tau^{\text{gb1}}$ (μs)                              | 3.9  | 4.1    | 3.7    | 4.3    | 4.8    |
|       | $f_0^{\text{gb1}}$ (MHz)                              | 0.041  | 0.039  | 0.043  | 0.0037 | 0.033  |
|       | $R^{\text{gb1}}$ (Ohm <sup>-1</sup> m <sup>-1</sup> ) | 301  | 473    | 336    | 235    | 173    |
|       | $C^{\text{gb1}}$ (nF)                                 | 12.3   | 14.3   | 37.2   | 53.3   | 50.1   |
|       | $\alpha_f^{\text{gb1}}$                               | 0.08   | 0.08   | 0.09   | 0.08   | 0.07   |
|       | $\alpha_R^{\text{gb1}}$                               | 0.28   | 0.41   | 0.40   | 0.29   | 0.27   |
|       | $\delta_0^{\text{gb1}}$ (nm)                          | 7.3  | 7.31   | 0.79   | 0.95   | 1.06   |
|       | $\tau^{\text{gb12}}$ (μs)                             | 39.6   | 39.6   | 39.6   | 59.2   | 79.1   |
| gb2   | $f_0^{\text{gb2}}$ (MHz)                              | 0.0040   | 0.0040 | 0.0040 | 0.0027 | 0.0020 |
|       | $R^{\text{gb2}}$ (Ohm <sup>-1</sup> m <sup>-1</sup> ) | 988  | 1005   | 923    | 1478   | 2771   |
|       | $C^{\text{gb2}}$ (μF)                                 | 1.05   | 0.48   | 0.65   | 0.65   | 0.36   |
|       | $\alpha_f^{\text{gb2}}$                               | 0.008  | 0.008  | 0.008  | 0.005  | 0.004  |
|       | $\alpha_R^{\text{gb2}}$                               | 0.56   | 0.59   | 0.64   | 0.72   | 0.85   |
|       | $\delta^{\text{gb2}}$ (nm)                            | 0.2  | 0.22   | 0.05   | 0.08   | 0.15   |
|       | $f_{\text{geo}}$                                      | 0.13   | 0.18   | 0.18   | 0.13   | 0.13   |

such systems. It confirmed SEM data and density measurements (Figs. 6a, 7a–d).

It was concluded that all ceramics have two grain boundary spaces that differ the geometries. The parameters of  $\alpha_f^{\text{gb1}}$  and  $\alpha_f^{\text{gb2}}$  practically did not depend on grain size less than 200 nm and decreased for systems that contained bigger grains. The parameters of  $\alpha_R^{\text{gb1}}$  and  $\alpha_R^{\text{gb2}}$  are non-monotonic changing with a maximum for ceramics with the grain size of 200–220 nm that show a higher density according to Fig. 6a. It is a good agreement with estimated values of grain boundary thicknesses. According to [31, 32, 79] the grain boundary thickness calculated as

$$\delta^{\text{gb}} = \frac{C^g}{C^{\text{gb}}} \cdot d_g. \quad (10)$$

Figure 9a shows  $\ln(\sigma T)$  versus  $1000/T_m$  dependences for grains ( $T_m$ —temperature of measurement),  $\sigma$  is calculated using the standard method according to (6) [57]. Linear approximation of these relations allows obtaining energy activation of ionic conductivity ( $E_a^g$ —grain activation energy,  $E_a^{\text{gb}}$ —grain boundary activation energy) as a slope to the  $X$ -axis. Figure 9b shows the changing the  $E_a^g$  from  $T_{\text{cal}}$  of NPs (or NPs size). According to data estimated from (6),  $E_a^g$  of

bulk oxygen diffusion doesn't change for all measured samples. It is evidence that forming a defective crystal structure of grain bulk depends on the sintering temperature values of ceramic. Energy activation of bulk ion diffusion ( $E = 0.9$  eV) is closed to estimated value for zirconia ceramic [80]. The  $E_a$  value of bulk oxygen diffusion varies from 0.8 to 1.0 eV depending on yttria contents in zirconia matrix.

Also, using Eq. (6), the activation energy values for ionic conductivity on grain boundary ( $E_a^{\text{gb}}$ ) are estimated. They are higher than bulk  $E_a$  and show a weak growth with the rising of grains sizes (NPs sizes used for ceramic sample manufacturing), see Fig. 9b. However, in some work [74], authors proposed the necessity of correction of  $\sigma$  values on grain boundary thickness in the framework of the bricklayer model because the defects amount in grain and intergrain space may be different.

Corrected  $\sigma$  named  $\sigma_{\text{sp}}$  is obtained according to

$$\sigma_{\text{gb}}^{\text{sp}} = \frac{L \cdot \delta^{\text{gb}}}{S \cdot d_g \cdot R^{\text{gb}}}. \quad (11)$$

After the correction of  $\sigma$  by  $\delta^{\text{gb}}$  the estimated  $E_a^{\text{gb}}$  values decreases ( $E_a^{\text{gb cor}}$ , see Fig. 9b, the correction values of  $E_a^{\text{gb cor}}$  are closed to  $E_a^g$ , especially for ceramic synthesized from NPs with  $T_{\text{cal}}$  in range 500–700 °C (NPs sizes are 12–18 nm). As

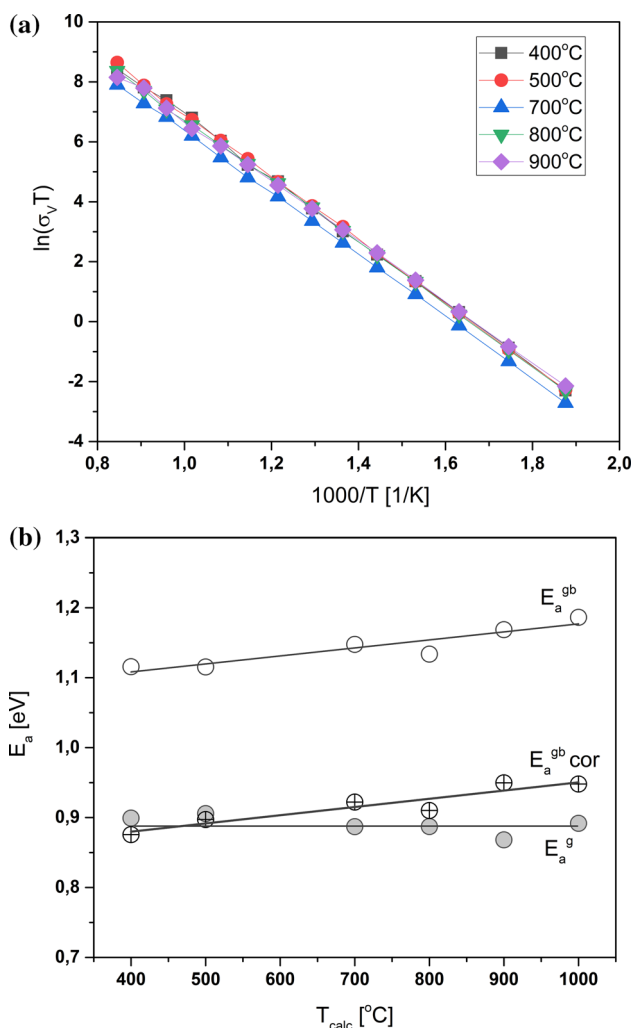


**Fig. 9** Dependences **a**  $\ln(\sigma T)$  versus  $1000/T$  for grains, **b** energy activation for processes in ceramic grain and boundary ( $E_a^g$  and  $E_a^{hg}$  estimated from approximations (6) and (11))

noted above, these ceramics have a higher densities (Fig. 6a). Thus, the ceramics based on NPs with small sizes show similar characteristics of grain and grain boundary spaces. NPs less than 20 nm in size can be recommended for the technology of zirconia ceramics used in energy applications.

### 3.3.3 Electrical Potential Generation in Y-Doped Zirconia Powders with Different Sizes in a Humid Atmosphere

Figure 10a presents the dependence of electrical potential which was generated in compact pressed from Y-doped zirconia powders with different sizes. The humidity of air was 80% at measurements. This dependence has non-monotonic characters with a maximum for a system with NPs size of 18 nm ( $T_{calc} = 700$  °C).

It is noted that the compacts from these NPs show higher green density that gives good contacts between NPs and

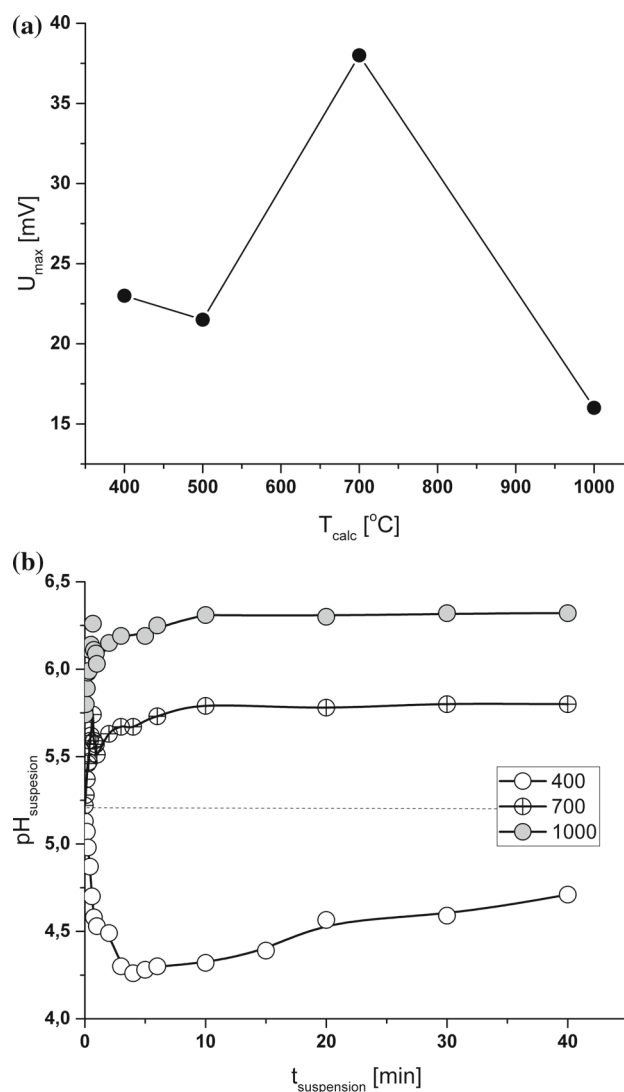


**Fig. 10** Influence of  $T_{calc}$  of NPs on **a** electric potential generation and **b** integral acidity to surface.  $pH_{suspension}$ —pH of suspension,  $t_{suspension}$ —time of suspension

determined porous space (Fig. 6b). The NPs surface state and types of the hydrated shell formed on NPs surface plays are essential in this electrophysical process. According to Fig. 6b, this NPs system shows low  $\zeta$ -potential. Powders with small sizes less 12 nm ( $T_{calc} = 400$ – $500$  °C) show similar values of water sorption. The increasing of NPs sizes leads decreasing of water sorption 3 and 10 times for NPs calcined at 700 (18 nm) and 1000 °C (35 nm) (Fig. 11a), but the  $S_{sa}$  values change in set of 115, 95, 49, 18  $m^2/g$  for pressed powders with  $T_{calc}$ : 400, 500, 700, and 1000 °C.

Figure 10b shows the integral surface acidity of NPs with different sizes ( $T_{calc}$ ). Data of pH-metry indicates changing of integral acidity from acidic (for NPs with  $T_{calc} = 400$ – $500$  °C) to close to neutral for NPs calcined at 700 °C and weakly basic for NPs calcined at 1000 °C. The presence

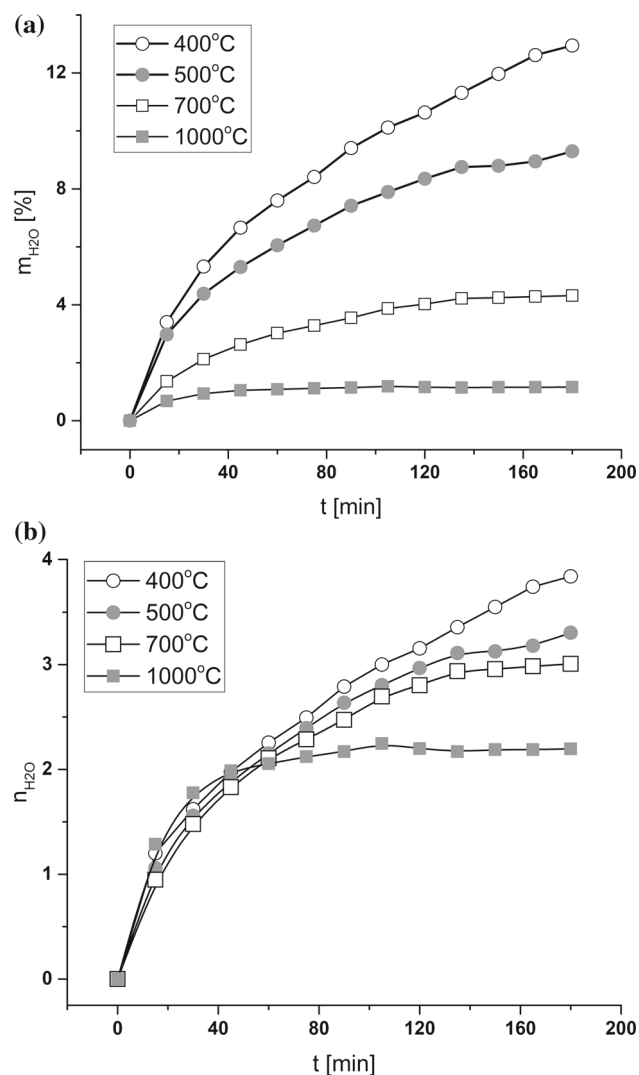


**Fig. 11** Kinetics of **a** water sorption and **b** water layer number on Zirconia NPs with different  $T_{cal}$  (NPs size).  $m_{H_2O}$ , Amount of adsorbed water (%),  $n_{H_2O}$ , Number of layer water,  $t$ , Adsorption time

of Lewis and Bronsted acidic and basic sites determines the NPS surface's integral acidity [52]. The basic properties of the surface appear for NPs with  $T_{cal} > 700$  °C when the basic Lewis and Bronsted sites begin to predominate [42], Figs. 6b and 10b. It leads to a difference in types of sorption characteristics of NPs and bonding strength of water molecules with surface. For NPs with acidic and basic sites on surfaces, water sorption occurs quickly on the beginning stage and molecules strongly connected with NPs surfaces for powders with  $T_{cal} = 400$  °C and 1000 °C. For NPs with  $T_{cal} = 700$  °C, water sorption in the beginning stage occurs more slowly due to less strength linking water with the surface. As a result, water is more labile on such NPs surface, and it dissociates to a lesser extent. It is confirmed by  $\zeta$ -potential values and integral acidity (Figs. 6b, 10b). It will be noted,

the forming of two water layers is observed for all NPs systems on the beginning stage of sorption. At the same time, the specific number of water layers in hydrated zirconia NPs decreases at the growth of NPs sizes (or  $T_{cal}$ ), Fig. 11b.

Thus, we can propose that the combinations of factors, namely a high density of green compact, integral acidity closed to neutral and low  $\zeta$ -potential value, are provided high ability to generate electric potential on compact powder sample.

## 4 Conclusion

The possibility of the organization of work in a physico-chemical laboratory in the SmartLab concept was shown. The laboratory is described as a module structure in which the block of synthesis is the main component. Protocol of synthesis of amorphous and crystalline zirconia with necessary functional properties is writing based on the understanding of crucial criteria for separate synthesis stage and marking the required feedback between powders producers and powders investigators and users. The scheme of working process organization is seen an example of the obtaining of materials for energy applications. In the described structure of a laboratory, nanomaterials' engineering for energy applications is optimized through "key parameter of synthesis—key structure criterion" link. It allows writing protocol of nanosized zirconia synthesis based on correlation I "zirconium salt concentration—powder dispersity" and correlation II "Calcined temperature—Nanoparticles sizes". It allows obtaining dispersive zirconia nanoparticles with predetermined sizes.

The correlation "material characteristics—material functionality" is built based on data of electrophysical properties of ceramic sintered from NPs with different sizes. It was shown that electrophysical properties of pressed green compacts and sintered ceramic correlate with their densities. It was shown that the ceramic density affects electrophysical properties more significantly than grain size.

It was shown that the use of powders with sizes 18–24 nm in technologies of SOFC and "humidity to electricity" is preferable. It is connected with the dispersity of such powder and their low surface potential that allows forming the pressed powder compacts and ceramics of high density needed for excellent electrophysical properties of zirconia.

**Acknowledgements** The authors are thankful the H2020-MSCA-RISE-2019 Program, project 871284 SSHARE for partial support of this work.

## Declarations

**Conflict of interest** The author declare that they have no conflict of interest.

## References

- Global Energy Transformation: A roadmap to 2050, International Renewable Energy Agency, Abu Dhabi. [www.irena.org/publications](http://www.irena.org/publications) (2019).
- Salameh, Z.: Renewable Energy System Design. Academic Press, San Diego (2014) <https://doi.org/10.1016/B978-0-12-374991-8.00001-5>
- Hussan, S.; Yanping, L.: Review of solid oxide fuel cell materials: cathode, anode and electrolyte. *Energy Trans.* **4**, 113–126 (2020). <https://doi.org/10.1007/s41825-020-00029-8>
- Zeng, J.; Xu, Y.; Yu, J.; Zhang, X., et al.: Compact yttria-stabilized zirconia based total NO<sub>x</sub> sensor with a dual functional Co<sub>3</sub>O<sub>4</sub>/NiO sensing electrode. *ACS Sens.* **4**, 2150–2155 (2019). <https://doi.org/10.1021/acssensors.9b00981>
- Shylo, A.; Doroshkevich, A.; Lyubchik, A.; Bacherikov, Yu., et al.: Electrophysical properties of hydrated porous dispersed system based on zirconia nanopowders. *Appl. Nanosci.* **10**, 4395–4402 (2020). <https://doi.org/10.1007/s13204-020-01471-2>
- Precious-Ayanwale, A.; Donohué-Cornejo, A.; Cuevas-González, J.C.; Espinosa-Cristóbal, L.F., et al.: Review of the synthesis, characterization and application of zirconia mixed metal oxide nanoparticles. *Int. J. Res. Granthaalayah.* **6**, 136–145 (2018). <https://doi.org/10.5281/zenodo.1403844>
- Kogut, I.; Wollbrink, A.; Wulfmeier, H.; El Azzouzi, F.-E., et al.: Linking the electrical conductivity and non-stoichiometry of thin film Ce<sub>1-x</sub>Zr<sub>x</sub>O<sub>2-δ</sub> by a resonant nanobalance approach. *Materials (Basel)*. **14**(4), 748 (2021). <https://doi.org/10.3390/ma14040748>
- Stub, S.; Vollestad, E.; Norby, T.: Protonic surface conduction controlled by space charge of intersecting grain boundaries in porous ceramics. *J. Mater. Chem.* **6**, 8265–8827 (2018). <https://doi.org/10.1039/c7ta11088j>
- Novoselov, I.; Karegin, A.; Shamanin, I.; Alyukov, E.; Gusev, A.: Plasmachemical synthesis of nanopowders of yttria and zirconia from dispersed water-salt-organic mixtures. *AIP Conf. Proc.* **1938**, 020010 (2018). <https://doi.org/10.1063/1.5027217>
- Vasyukiv, O.; Sakka, Y.: Synthesis and sintering of zirconia nanopowder by non-isothermal decomposition from hydroxide. *J. Ceram. Soc. JAPAN* **109**, 500–505 (2001). [https://doi.org/10.2109/jcersj.109.1270\\_500](https://doi.org/10.2109/jcersj.109.1270_500)
- Tsuzuki, T.: Mechanochemical synthesis of metal oxide nanoparticles. *Commun. Chem.* **4**(143), 1–11 (2021). <https://doi.org/10.1038/s42004-021-00582-3>
- Dahiya, M.S.; Tomer, U.K.; Duhan, S.: Metal–ferrite nanocomposites for targeted drug delivery. In: Asiri, A.M.; Inamudin, D.; Mohammad, A. (Eds.) *Applications of nanocomposite materials in drug delivery*, pp. 737–760. Woodhead Publishing, Berlin (2018). <https://doi.org/10.1016/B978-0-12-813741-3.00032-7>
- Zirconia. Tosoh corporation, Tokyo. <https://www.rbhld.com/wp-content/uploads/2019/05/Tosoh-Zirconia-Brochure.pdf> (2019)
- Leib, E.W.; Pasquarelli, R.M.; Blankenburg, M.; Muller, M.; Schreyer, A., et al.: High-temperature stable zirconia particles doped with yttrium, lanthanum, and gadolinium. Part. Part. Syst. Charact. **33**, 645–655 (2016). <https://doi.org/10.1002/ppsc.201600069>
- Charitidis, C.A.; Georgiou, P.; Koklioti, M.A.: Manufacturing nanomaterials: from research to industry. *Manuf. Rev.* **1**(11), 1–19 (2014). <https://doi.org/10.1051/mfreview/2014009>
- Phan, H.T.; Haes, A.J.: What does nanoparticle stability mean? *J. Phys. Chem. C Nanometer Interfaces* **123**(27), 16495–16507 (2019). <https://doi.org/10.1021/acs.jpcc.9b00913>
- Jeong, Y.-S.; Chin, S.H.: Synthesis and characterization of high surface area of Zirconia: effect of pH. *Korean Chem. Eng. Res.* **57**, 133–141 (2019). <https://doi.org/10.9713/kcer.2019.57.1.133>
- Huang, Z.; Han, W.; Feng, Z.; Qi, J.; Wu, D., et al.: The effects of precipitants on coprecipitation synthesis of yttria-stabilized zirconia nanocrystalline powders. *J. Sol Gel Sci. Technol.* **90**, 359–368 (2019). <https://doi.org/10.1007/s10971-019-04947-y>
- Jang, W.; Yun, J.; Ludwig, L.; Jang, S.G.; Bae, J.Y., et al.: Comparative catalytic properties of supported and encapsulated gold nanoparticles in homocoupling reactions. *Front. Chem.* **8**(834), 1–9 (2020). <https://doi.org/10.3389/fchem.2020.00834>
- León, B.; Albano, M.P.; Stábile, F.M.; Garrido, L.B.: Processing of concentrated aqueous zirconia-bioglass slips by slip casting. *Ceramics-Silikáty* **61**(2), 91–98 (2017). <https://doi.org/10.13168/cs.2017.0002>
- Kim, H.J.; Kim, M.; Neoh, K.C., et al.: Slurry spin coating of thin film yttria stabilized zirconia/gadolinia doped ceria bi-layer electrolytes for solid oxide fuel cells. *J. Power Sources* **327**, 401–407 (2016). <https://doi.org/10.1016/j.jpowsour.2016.07.080>
- Obal, K.; Wyrwa, J.; Kruk, A.; Dziubaniuk, M., et al.: Microstructure and electrical conductivity of 3Y-TZP/Al<sub>2</sub>O<sub>3</sub> composites. *Process. Appl. Ceram.* **15**, 19–31 (2021). <https://doi.org/10.2298/PAC21010190>
- Mahato, N.; Banerjee, A.; Gupta, A.; Omar, S.; Balani, K.: Progress in material selection for solid oxide fuel cell technology: a review. *Prog. Mater. Sci.* **72**, 141–337 (2015). <https://doi.org/10.1016/j.pmatsci.2015.01.001>
- Daza, P.C.C.; Meneses, R.A.M.; Ferreira, J.L.A.: Influence of microstructural characteristics on ionic conductivity of ceria based ceramic solid electrolytes. *Ceram. Int.* **44**, 2138–2145 (2018). <https://doi.org/10.1016/j.ceramint.2017.10.166>
- Xue, Q.; Huang, X.; Zhang, J.; Zhang, H.; Feng, Z.: Grain boundary segregation and its influences on ionic conduction properties of scandia doped zirconia electrolytes. *J. Rare Earth* **37**, 645–651 (2019). <https://doi.org/10.1016/j.jre.2018.11.006>
- Cheikh, A.; Madani, A.; Touati, A.; Boussetta, H.; Monty, C.: Ionic conductivity of zirconia based ceramics from single crystals to nanostructured polycrystals. *J. Eur. Ceram. Soc.* **21**, 1837–1841 (2001). [https://doi.org/10.1016/S0955-2219\(01\)00126-1](https://doi.org/10.1016/S0955-2219(01)00126-1)
- Priya, S.D.; Selvakumar, A.I.; Nesaraj, A.S.: Overview on ceramic and nanostructured materials for solid oxide fuel cells (SOFCs) working at different temperatures. *J. Electrochem. Sci. Tech.* **11**, 99–116 (2020). <https://doi.org/10.33961/jecst.2019.00612>
- Arena, A.; Prete, F.; Rambaldi, E.; Bignozzi, M.C.; Monaco, C., et al.: Nanostructured zirconia-based ceramics and composites in dentistry: a state-of-the-art review. *Nanomaterials (Basel)*. **10**(9), 1393 (2019). <https://doi.org/10.3390/nano9101393>
- Tao, J.; Dong, A.; Wang, J.: The influence of microstructure and grain boundary on the electrical properties of scandia stabilized zirconia. *Mater. Trans.* **54**, 825–832 (2013). <https://doi.org/10.2320/matertrans.M2012385>
- Durá, O.J.; López de la Torre, M.A.; Vázquez, L., et al.: Ionic conductivity of nanocrystalline yttria-stabilized zirconia: grain boundary and size effects. *Phys. Rev. B*. **81**, 184301 (2010). <https://doi.org/10.1103/PhysRevB.81.184301>
- Vikrant, K.S.N.; García, R.E.: Charged grain boundary transitions in ionic ceramics for energy applications. *npj Comput. Mater.* **5**, 24 (2019). <https://doi.org/10.1038/s41524-019-0159-2>
- Hwang, J.H.; McLachlan, D.S.; Mason, T.O.: Brick layer model analysis of nanoscale-to-microscale cerium dioxide. *J. Electroceram.* **3**, 7–16 (1999). <https://doi.org/10.1023/A:1009998114205>
- Maca, K.; Trunek, M.: Compaction and pressureless sintering of zirconia nanoparticles. *J. Am. Ceram. Soc.* **90**, 2735–2740 (2007). <https://doi.org/10.1111/j.1551-2916.2007.01781.x>
- Abdullah, B.J.; Jiang, Q.; Omar, M.S.: Effects of size on mass density and its influence on mechanical and thermal properties of ZrO<sub>2</sub> nanoparticles in different structures. *Bull. Mater. Sci.* **39**, 1295–1302 (2016). <https://doi.org/10.1007/s12034-016-1244-5>



35. Ghosh, A.; Dey, G.K.; Suri, A.K.: Correlation of electrical conductivity with microstructure in 3Y-TZP System: From nano to submicrometer grain size range. *J. Am. Ceram. Soc.* **91**(11), 3768–3770 (2008). <https://doi.org/10.1111/j.1551-2916.2008.02696.x>
36. Dura, O.J.; De la Torre, L.; Chaboy, V.J.; Boada, R., et al.: Ionic conductivity of nanocrystalline yttria-stabilized zirconia: grain boundary and size effects. *Phys. Rev. B* **81**, 184301 (2010). <https://doi.org/10.1103/PhysRevB.81.184301>
37. Kazlauskas, S.; Kazakevičius, E.; Zalga, A.; Daugėla, S.; Kežionis, A.: Peculiarities of charge carrier relaxation in grain boundary of gadolinium-doped ceria ceramics. *Lith. J. Phys.* **59**, 94–103 (2019)
38. Miyoshi, S.; Akao, Y.; Kuwata, N.; Kawamura, J.; Oyama, Y., et al.: Low-temperature protonic conduction based on surface protonics: an example of nano-structured yttria-doped zirconia. *Chem. Mater.* **26**, 5194–5200 (2014). <https://doi.org/10.1021/cm5012923>
39. Doroshkevich, A.S.; Asgerov, E.B.; Shylo, A.V.; Lyubchik, A.I., et al.: Direct conversion of the water adsorption energy to electricity on the surface of zirconia nanoparticles. *Appl. Nanosci.* **9**, 1603–1609 (2019). <https://doi.org/10.1007/s13204-019-00979-6>
40. Sun, Z.; Wen, X.; Wang, L.; Ji, D.; Qin, X., et al.: Emerging design principles, materials, and applications for moisture-enabled electric generation. *eScience* (2022). <https://doi.org/10.1016/j.esci.2021.12.009>
41. Huang, Y.; Cheng, H.; Yang, C.; Zhang, P.; Liao, Q., et al.: Interface-mediated pyroelectric generator with an output voltage approaching 1.5 volts. *Nat. Commun.* **9**, 4166 (2018). <https://doi.org/10.1038/s41467-018-06633-z>
42. Danilenko, I.; Gorban, O.; Shylo, A.; Volkova, G., et al.: Humidity to electricity converter based on oxide nanoparticles. *J. Mater. Sci.* (2022). <https://doi.org/10.1007/s.10853-021-06657-9>
43. Shylo, A.; Danilenko, I.; Gorban, O.; Doroshkevich, O., et al.: Hydrated zirconia nanoparticles as media for electrical charge accumulation. *J. Nanopart. Res.* **24**, 18 (2022). <https://doi.org/10.1007/s11051-022-05407-5>
44. Konstantinova, T.; Danilenko, I.; Glazunova, V.; Volkova, G.; Gorban, O.: Mesoscopic phenomena in oxide nanoparticles systems: processes of growth. *J. Nanopart. Res.* **13**, 4015–4023 (2011). <https://doi.org/10.1007/s11051-011-0329-8>
45. Gorban, O.; Synyakina, S.; Volkova, G.; Kulik, Y.; Konstantinova, T.: Surface influence on the behavior of stabilized zirconia nanoparticles under pressure. *High Press. Res.* **32**, 72–80 (2012). <https://doi.org/10.1080/08957959.2012.655245>
46. Azhar, O.; Jahan, Z.; Sher, F.; Niazi, M.B.K., et al.: Cellulose acetate-polyvinyl alcohol blend hemodialysis membranes integrated with dialysis performance and high biocompatibility. *Mater. Sci. Eng. C.* **126**, 112–127 (2021). <https://doi.org/10.1016/j.msec.2021.112127>
47. Sani, E.; Mercatelli, L.; Sans, J.-L.; Sciti, D.: Optical properties of black and white ZrO<sub>2</sub> for solar receiver applications. *Solar Energy Mater. Solar Cells* **140**, 477–482 (2015). <https://doi.org/10.1016/j.solmat.2015.02.007>
48. Al-Rawi, U.A.; Sherb, F.; Hazafa, A.; Bilala, M., et al.: Synthesis of Zeolite supported bimetallic catalyst and application in n-hexane hydro-isomerization using supercritical CO<sub>2</sub>. *J. Environ. Chem. Eng.* **9**(4), 105206 (2021). <https://doi.org/10.1016/j.jece.2021.105206>
49. Frey, J.G.: Dark lab or smart lab: the challenges for 21st century laboratory software. *Org. Proc. Res. Dev.* **8**, 1024–1035 (2004). <https://doi.org/10.1021/op049895g>
50. Brunauer, S.; Emmett, P.H.; Teller, E.: Adsorption of gases in multimolecular layers. *J. Am. Chem. Soc.* **60**(2), 309–319 (1938). <https://doi.org/10.1021/ja01269a023>
51. Galarneau, A.; Mehlhorn, D.; Guenneau, F.; Coasne, B., et al.: Specific surface area determination for microporous/mesoporous materials: the case of mesoporous FAU-Y zeolites. *Langmuir ACS.* **34**(47), 14134–14142 (2018). <https://doi.org/10.1021/acs.langmuir.8b02144>
52. Geffert, A.; Geffertova, J.; Dudiak, M.: Direct method of measuring the pH value of wood. *Forests* **10**(1–9), 852 (2019). <https://doi.org/10.3390/f10100852>
53. Plohl, O.; Zemljic, L.F.; Potrc, S.; Luxbacher, T.: Applicability of electro-osmotic flow for the analysis of the surface zeta potential. *RSC Adv.* **10**, 6777–6789 (2020). <https://doi.org/10.1039/C9RA10414C>
54. Ivers-Tiffée, E.; Weber, A.: Evaluation of electrochemical impedance spectra by the distribution of relaxation times. *J. Ceram. Soc. Jpn.* **125**, 193–201 (2017). <https://doi.org/10.2109/jcersj2.16267>
55. Ciuccia, F.; Chena, C.: Analysis of electrochemical impedance spectroscopy data using the distribution of relaxation times: a Bayesian and hierarchical Bayesian approach. *Electrochim. Acta* **167**, 439–454 (2015). <https://doi.org/10.1016/j.electacta.2015.03.123>
56. Barsoukov, E.; Macdonald, J.R.: Impedance Spectroscopy. Theory. Experiment and Application. Wiley-Interscience, New York (2005) <https://doi.org/10.1002/9781119381860>
57. Schlupp, M.V.F.; Scherrer, B.; Ma, H.; Grolig, J.G., et al.: Influence of microstructure on the cross-plane oxygen ion conductivity of yttria stabilized zirconia thin films. *Phys. Status Solidi A.* **209**, 1–9 (2012). <https://doi.org/10.1002/pssa.201228248>
58. Dietz, J.: Enterprise Ontology—Theory and Methodology. Springer, Berlin (2006) <https://doi.org/10.1007/3-540-33149-2>
59. Krishna Sarenda, M.; Annaporani, S.; Ansar, E.B.; Harikrishna Varma, P.R., et al.: Magnetic hydrotremia studies on water-soluble polyacrylic acid-coated cobalt ferrite nanoparticles. *J. Nanopart. Res.* **16**, 2773 (2014). <https://doi.org/10.1007/s11051-014-2773-8>
60. Pilipenko, N.P.; Konstantinova, T.E.; Tokiy, V.V.; Danilenko, I.A., et al.: Peculiarities of zirconium hydroxide microwave drying process. *Funct. Mater.* **2**, 545–548 (2002)
61. Gorban, O.A.; Synyakina, S.A.; Kulik, Yu.O.; Ryumshina, T.A., et al.: Structural evolution of the ZrO<sub>2</sub>–Y<sub>2</sub>O<sub>3</sub> nanoparticulate xerogels under high hydrostatic pressure. *Funct. Mater.* **17**(40), 1–6 (2010)
62. Ivanov, V.K.; Baranchikov, A.Y.; Kopitsa, G.P.; Lermontov, S.A.; Yurkova, L.L., et al.: pH control of the structure, composition, and catalytic activity of sulfated zirconia. *J. Solid State Chem.* **198**, 496–505 (2013). <https://doi.org/10.1016/j.jssc.2012.11.022>
63. Tao, K.; Dou, H.; Sun, K.: Interfacial coprecipitation to prepare magnetite nanoparticles: concentration and temperature dependence. *Colloids Surf. A Physicochem. Eng. Asp.* **320**, 115–122 (2008). <https://doi.org/10.1016/j.colsurfa.2008.01.051>
64. Galarneau, A.; Villemot, F.; Rodriguez, J.; Fajula, F.; Coasne, B.: Validity of the t-plot method to assess microporosity in hierarchical micro/mesoporous materials. *Langmuir* **30**, 13266–13274 (2014). <https://doi.org/10.1021/la5026679l>
65. Wohlleben, W.; Mielke, J.; Bianchin, A.; Ghanem, A., et al.: Reliable nanomaterial classification of powders using the volume-specific surface area method. *J. Nanopart. Res.* **19**, 61 (2017). <https://doi.org/10.1007/s11051-017-3741-x>
66. Green, M.C.; Taylor, R.; Moeser, G.D.; Kyrilidis, A.; Sawka, R.M.: Mesoporous carbon black and processes making same. Patent USA, US 2009/0208751 A1 Aug. 20 (2009)
67. Sinelnikova, S.; Volkova, G.; Gorban, O.: Influence of dopant amount on evolution of zirconia crystal energy. Non-equilibrium phase transformations. *Int. Sci. J. Mater. Sci.* **1**, 7–10 (2016)
68. Sameut-Bouhaik, I.; Leroy, P.; Ollivier, P.; Azaroual, M.; Mercury, L.: Influence of surface conductivity on the apparent zeta potential of TiO<sub>2</sub> nanoparticles: application to the modeling of their aggregation kinetics. *J. Colloid Interface Sci.* **406**, 75–85 (2013). <https://doi.org/10.1016/j.jcis.2013.05.034>





69. Muccillo, R.; Muccillo, E.N.S.: Electric field assisted sintering of electroceramics and in situ analysis by impedance spectroscopy. *J. Electroceram.* **38**, 24–42 (2017). <https://doi.org/10.1007/s10832-016-0054-x>
70. Yavarinasab, A.; Janfaza, S.; Tahmooressi, H.; Ghazi, M., et al.: A selective polypyrrole-based sub-ppm impedimetric sensor for the detection of dissolved hydrogen sulfide and ammonia in a mixture. *J. Hazard Mater.* **416**, 125892 (2021). <https://doi.org/10.1016/j.jhazmat.2021.125892>
71. Kežionis, A.; Kazlauskas, S.; Petruionis, D.; Orliukas, A.F.: Relationship between charge carrier relaxation and peculiarities of electric response in some solid oxygen ion conductors. *Solid State Ion.* **279**, 25–31 (2015). <https://doi.org/10.1016/j.ssi.2015.07.009>
72. Yavarinasab, A.; Janfaza, S.; Tasnim, N.; Tahmooressi, H., et al.: Graphene/poly (methyl methacrylate) electrochemical impedance-transduced chemiresistor for detection of volatile organic compounds in aqueous medium. *Anal. Chim. Acta* **1109**, 27–36 (2020). <https://doi.org/10.1016/j.aca.2020.02.065>
73. McNealy, B.E.; Hertz, J.L.: On the use of the constant phase element to understand variation in grain boundary properties. *Solid State Ionics* **256**, 52–60 (2014). <https://doi.org/10.1016/j.ssi.2013.12.030>
74. Kusnezof, M.; Wagner, D.; Schilm, J.; Heubner, C., et al.: Influence of microstructure and crystalline phases on impedance spectra of sodium conducting glass ceramics produced from glass powder. *J. Solid State Electrochem.* **26**, 375–388 (2022). <https://doi.org/10.1007/s10008-021-05063-0>
75. Osinkin, D.; Antonova, A.; Lesnichyova, A.; Tropin, E.: Application of promising electrode materials in contact with a thin-layer ZrO<sub>2</sub>-based supporting electrolyte for solid oxide fuel cells. *Energies* **13**(5), 1190 (2020). <https://doi.org/10.3390/en13051190>
76. Deportes, C.; Duclot, M.; Fabry, P.; Fouletier, J., et al.: *Electrochimie des Solides*. Grenoble Sciences, Grenoble (2008) <https://doi.org/10.1051/978-2-7598-1216-5>
77. Irvine, J.T.S.; Sinclair, D.C.; West, A.R.: Electroceramics: characterization by impedance spectroscopy. *J. Adv. Mater.* **2**(3), 138–192 (1990). <https://doi.org/10.1002/adma.19900020304>
78. Kleitz, M.; Dessemond, L.; Steil, M.C.: Model for ion-blocking at internal interfaces in zirconias. *Solid State Ion.* **75**, 107–115 (1995). <https://doi.org/10.1016/j.pmatsci.2005.07.001>
79. Guo, X.; Waizer, R.: Electrical properties of the grain boundaries of oxygen ion conductors: acceptor-doped zirconia and ceria. *Prog. Mater. Sci.* **51**, 151–210 (2006). <https://doi.org/10.1016/j.pmatsci.2005.07.001>
80. Kilo, M.; Argirusis, C.; Borchardt, G.; Jackson, R.A.: Oxygen diffusion in yttria stabilized zirconia—experimental results and molecular dynamics calculations. *Phys. Chem. Chem. Phys.* **5**, 2219–2224 (2003). <https://doi.org/10.1039/b300151m>

